

# UC Berkeley

## UC Berkeley Previously Published Works

### Title

Direct Visualization of the Interfacial Degradation of Cathode Coatings in Solid State Batteries: A Combined Experimental and Computational Study

### Permalink

<https://escholarship.org/uc/item/4wb8w0g4>

### Journal

Advanced Energy Materials, 10(27)

### ISSN

1614-6832

### Authors

Zhang, Ya-Qian

Tian, Yaosen

Xiao, Yihan

et al.

### Publication Date

2020-07-01

### DOI

10.1002/aenm.201903778

Peer reviewed

# Direct Visualization of the Interfacial Degradation of Cathode Coatings in Solid State Batteries: A Combined Experimental and Computational Study

Ya-Qian Zhang, Yaosen Tian, Yihan Xiao, Lincoln J. Miara, Yuichi Aihara, Tomoyuki Tsujimura, Tan Shi, M. C. Scott,\* and Gerbrand Ceder\*

The interfacial instability between a thiophosphate solid electrolyte and oxide cathodes results in rapid capacity fade and has driven the need for cathode coatings. In this work, the stability, evolution, and performance of uncoated,  $\text{Li}_2\text{ZrO}_3$ -coated, and  $\text{Li}_3\text{B}_{11}\text{O}_{18}$ -coated  $\text{LiNi}_{0.5}\text{Co}_{0.2}\text{Mn}_{0.3}\text{O}_2$  cathodes are compared using first-principles computations and electron microscopy characterization.  $\text{Li}_3\text{B}_{11}\text{O}_{18}$  is identified as a superior coating that exhibits excellent oxidation/chemical stability, leading to substantially improved performance over cells with  $\text{Li}_2\text{ZrO}_3$ -coated or uncoated cathodes. The chemical and structural origin of the different performance is interpreted using different microscopy techniques which enable the direct observation of the phase decomposition of the  $\text{Li}_2\text{ZrO}_3$  coating. It is observed that Li is already extracted from the  $\text{Li}_2\text{ZrO}_3$  in the first charge, leading to the formation of  $\text{ZrO}_2$  nanocrystallites with loss of protection of the cathode. After 50 cycles separated (Co, Ni)-sulfides and Mn-sulfides can be observed within the  $\text{Li}_2\text{ZrO}_3$ -coated material. This work illustrates the severity of the interfacial reactions between a thiophosphate electrolyte and oxide cathode and shows the importance of using coating materials that are absolutely stable at high voltage.


## 1. Introduction

Solid-state batteries (SSBs) have received considerable attention owing to their reduced flammability and the ability to use high-energy-density metal anodes compared with those of liquid-electrolyte battery systems.<sup>[1,2]</sup> Substantial progress has been achieved in the development of SSBs, with particular effort focused on identifying solid superionic conductors. Among

known inorganic solid electrolytes (SEs), thiophosphates offer the advantage of combining high ionic conductivity with low cost and ease of processing, making them strong candidates for large-scale applications.<sup>[3,4]</sup> However, both ab initio computations and experimental studies indicate that thiophosphate SEs and commonly used oxide cathode materials are not stable in contact with each other.<sup>[5–9]</sup> This interfacial instability leads to increased resistance during cycling,<sup>[7,10–12]</sup> resulting in capacity fade and poor rate performance, indicating the need for interface engineering in SSBs.

To suppress the reaction between the cathode and thiophosphate SEs, various cathode coating materials have been developed to serve as a buffer layer and prevent direct contact between the cathode and SE.<sup>[13,14]</sup> Most investigations on cathode coatings in thiophosphate-based SSBs have focused on exploring ternary metal oxides<sup>[13]</sup> such as  $\text{LiNbO}_3$ ,<sup>[12,15,16]</sup>  $\text{LiTaO}_3$ ,<sup>[17]</sup> and  $\text{Li}_2\text{ZrO}_3$  (LZrO),<sup>[18,19]</sup> However, such coating materials do not completely solve the interfacial issue between the cathode and SE. For example, despite the reduced interfacial resistance and enhanced capacity retention achieved in SSBs using  $\text{LiNb}_x\text{Ta}_{1-x}\text{O}_3$  coatings, Co diffusion from the  $\text{LiCoO}_2$  cathode to the thin film coating is still observed.<sup>[12,20]</sup> First-principles computation also indicates that the high binding energy of a  $\text{PO}_4$  group creates a driving force for S/O exchange between  $\text{LiNbO}_3$ ,  $\text{LiTaO}_3$ , and

Dr. Y.-Q. Zhang, Dr. Y. Tian, Y. Xiao, Dr. T. Shi, Prof. M. C. Scott, Prof. G. Ceder  
Department of Materials Science and Engineering  
University of California Berkeley  
Berkeley, CA 94720, USA  
E-mail: mary.scott@berkeley.edu; gceder@berkeley.edu

 The ORCID identification number(s) for the author(s) of this article can be found under <https://doi.org/10.1002/aenm.201903778>.

© 2020 The Authors. Published by WILEY-VCH Verlag GmbH & Co. KGaA, Weinheim. This is an open access article under the terms of the Creative Commons Attribution License, which permits use, distribution and reproduction in any medium, provided the original work is properly cited.

The copyright line for this article was changed on 30 June 2020 after original online publication.

DOI: 10.1002/aenm.201903778

Dr. Y.-Q. Zhang, Prof. M. C. Scott  
The Molecular Foundry  
Lawrence Berkeley National Laboratory  
Berkeley, CA 94720, USA

Dr. Y. Tian, Y. Xiao, Dr. T. Shi, Prof. G. Ceder  
Materials Sciences Division  
Lawrence Berkeley National Laboratory  
Berkeley, CA 94720, USA

Dr. L. J. Miara  
Advanced Materials Lab  
Samsung Research America  
Burlington, MA 01803, USA

Dr. Y. Aihara, Dr. T. Tsujimura  
Samsung R&D Institute Japan  
Osaka 562-0036, Japan

LZrO coatings and thiophosphate SEs.<sup>[14,21]</sup> In addition, the relatively low oxidation limit of these ternary-metal-oxide coatings raises concern for their stability at high voltages.<sup>[14,21]</sup>

An ideal coating material, therefore, requires a wide stability window that spans the cathode operating voltage and has low reactivity with both cathode and SE. Recently, with the aid of first-principles computation, lithium borates have been identified as a promising class of cathode coating materials that combine low reactivity with oxide cathodes and thiophosphate SEs with good oxidation stability.<sup>[14,22]</sup> Although computational screening has provided an efficient way to identify ideal compositions with targeted properties, experimental validation, and direct observations of how different coatings behave in a certain (electro-)chemical environments is crucial for the development of new coatings. Various methods have been established to investigate interfaces in liquid-electrolyte battery systems; however, obstacles remain in studying the interface behavior in SSBs, in part because of the difficulty of isolating an intact solid/solid interface in SSBs.<sup>[11]</sup> The characterization of the complex interparticle interfaces is further hindered by the nanosized length scale, air sensitivity, and amorphous nature of some decomposition products.<sup>[5,23]</sup> Advanced (scanning) transmission electron microscopy ((S)TEM) analysis with air-free sample preparation and transfer enables accurate probing of the chemical/structure evolution of the solid-state interfaces in SSBs.<sup>[7,11]</sup> In this paper, we combine different microscopy techniques (imaging and spectroscopy) to probe the chemical composition and microstructure of cathode composite interfaces with nanoscale resolution.

In this work, we select the lithium borate  $\text{Li}_3\text{B}_{11}\text{O}_{18}$  (LBO) for detailed investigation because of its high oxidation stability limit and good chemical compatibility with both layered oxide cathode  $\text{LiNi}_{0.5}\text{Co}_{0.2}\text{Mn}_{0.3}\text{O}_2$  (NCM<sup>523</sup>) and glassy  $\text{Li}_3\text{PS}_4$  (LPS) thiophosphate SE. Electrochemical methods were used to test the coating's effect on the discharge capacity and cycle-life of the SSB full cells. One commonly used ternary metal oxide coating, LZrO, which is predicted to be unstable at high voltage, was also characterized for comparison purposes to help identify the factors contributing to the coating stability.<sup>[14]</sup> Compared with the uncoated and LZrO-coated NCM<sup>523</sup>, the LBO-coated NCM<sup>523</sup> exhibits a greatly improved discharge capacity and capacity retention. The chemical and structural origin of the differences observed in the electrochemical behavior are interpreted using (S)TEM to observe the coatings and interfaces present in the cathode composite. Our combined computational and microscopic study helps to elucidate the critical coating parameters and provides a general methodology for future coating development and interface characterization in SSBs.

## 2. Results

### 2.1. Density Functional Theory (DFT) Computation of Coating Stability

The electrochemical stability window of a material and the decomposition products at a given Li chemical potential can be predicted using a first-principles methodology previously developed.<sup>[5,24,25]</sup> The thermodynamic stability window represents

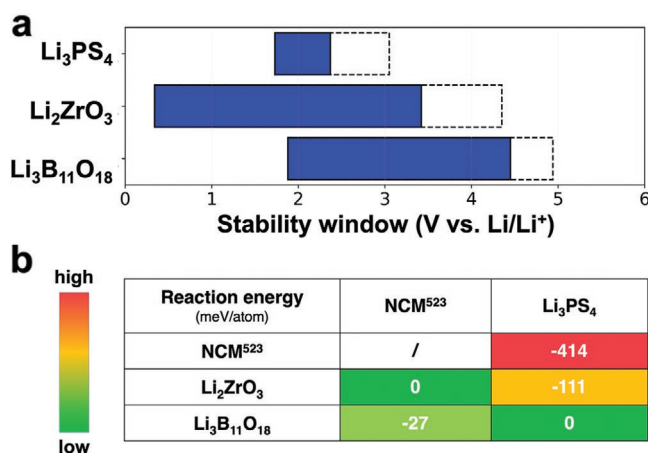


**Figure 1.** DFT computation of stability of  $\text{Li}_2\text{ZrO}_3$  (LZrO) and  $\text{Li}_3\text{B}_{11}\text{O}_{18}$  (LBO) coatings. a) Stability window of LPS, LZrO, and LBO. The blue-filled area represents the thermodynamic stability window and the window indicated by the dashed lines represents the maximal extended kinetic oxidation limit. b) Chemical reactivity energies (in meV per atom) of reaction pairs among NCM<sup>523</sup>, LPS, LZrO, and LBO. Negative values indicate a driving force for reaction.

the “safe” voltage range, over which there is no driving force for decomposition, whereas the oxidation limit at which a  $\text{Li}^+$  ion and an electron can be topotactically extracted from a material represents the absolute upper voltage limit for kinetic stabilization.<sup>[25]</sup> Detailed descriptions of the computation methods are provided in previous work and in the Experimental Section.<sup>[5,24,25]</sup> The stability limits of LPS, LZrO, and LBO are summarized in **Figure 1a** and Table S1 in the Supporting Information.

As observed in **Figure 1a**, the stability windows of both LZrO and LBO overlap with that of LPS. However, the two coatings have divergent stabilities at  $\approx 4.3$  V versus  $\text{Li}/\text{Li}^+$ . LZrO is predicted to become thermodynamically unstable at 3.42 V. Although the stability window can be kinetically expanded, LZrO will likely undergo decomposition within the common operating voltage window of NCM<sup>523</sup> cathode (e.g., 2.5–4.3 V). When charged to 4.3 V or higher, LZrO is likely oxidized by Li extraction via the predicted decomposition reaction expressed in Equation (1). In contrast, LBO exhibits a higher thermodynamic oxidation limit of 4.45 V due to the strong hybridization between boron and oxygen,<sup>[14]</sup> indicating that the LBO coating is likely to remain stable over the entire battery cycling voltage range of 2.5–4.3 V.



We also considered the chemical stability at the cathode/SE, cathode/coating, and coating/SE interfaces (**Figure 1b**). With no buffer layer, a high reactivity of  $-414$  meV per atom is predicted between discharged NCM<sup>523</sup> and LPS, indicating a highly unstable interface upon direct contact. Both LZrO and LBO coatings exhibit significantly reduced reaction driving forces with NCM<sup>523</sup> (0 meV per atom for LZrO and  $-27$  meV per atom for LBO). For the LPS/coating interface, a non-negligible driving force exists between the LZrO coating and LPS ( $-111$  meV per atom) to form  $\text{Li}_3\text{PO}_4$ , whereas LBO is

thermodynamically stable in contact with LPS. Therefore, LBO is expected to act as a chemically more robust barrier layer at the NCM<sup>523</sup>/LPS interface than LZrO, and provides a wide stability window spanning the voltage range of typical NCM<sup>523</sup> cathodes. A full list of the computed reactivities and the predicted reactions of all the reaction pairs is provided in Table S2 in the Supporting Information.

## 2.2. Effectiveness of LZrO and LBO Coatings

To experimentally investigate the stability and effectiveness of the two coatings, both LBO-coated and LZrO-coated NCM<sup>523</sup> were prepared using sol-gel coating methods as described in the Experimental Section. Electron microscopy images of the uncoated/coated NCM<sup>523</sup> particles are presented in **Figure 2**. As observed in the scanning electron microscopy (SEM) images in the top three panels of **Figure 2**, the morphology of the NCM<sup>523</sup> secondary particles is preserved after the coating process. TEM and high-resolution transmission electron microscopy (HRTEM) images indicate that the uncoated NCM<sup>523</sup> particle

has a clean surface with lattice fringes extending to the particle edge (**Figure 2b,c**). As observed in the TEM and HRTEM images in **Figure 2e,f** (for the LZrO-coated NCM<sup>523</sup>) and **Figure 2h,i** (for the LBO-coated NCM<sup>523</sup>), a thin and uniform coating layer ranging from a few nanometers to  $\approx 10$  nm in thickness is observed on the surface of the NCM<sup>523</sup> particles. The HRTEM images in **Figure 2f,i** reveal amorphous features for both the LZrO and LBO coatings.

Full-cell SSBs using the uncoated/coated NCM<sup>523</sup> cathodes were constructed and cycled at a constant current ( $0.1 \text{ mA cm}^{-2}$  for charge and  $0.05 \text{ mA cm}^{-2}$  for discharge) between 2.5 and 4.3 V versus Li/Li<sup>+</sup> to evaluate the effectiveness of the LBO and LZrO coatings. The cells were assembled in an Ar atmosphere using identical procedures; LPS powder from the same batch was used to maximize consistency. **Figures S1–S3** in the Supporting Information show the representative charge–discharge curves of uncoated, LBO and LZrO-coated NCM<sup>523</sup> in the SSBs. **Figure 3** presents the discharge capacity and capacity retention of the cells for the first 100 cycles. Among all the cells constructed, the uncoated NCM<sup>523</sup> cathode exhibits the lowest discharge capacity ( $107.1 \text{ mAh g}^{-1}$  in the 1st cycle) and the

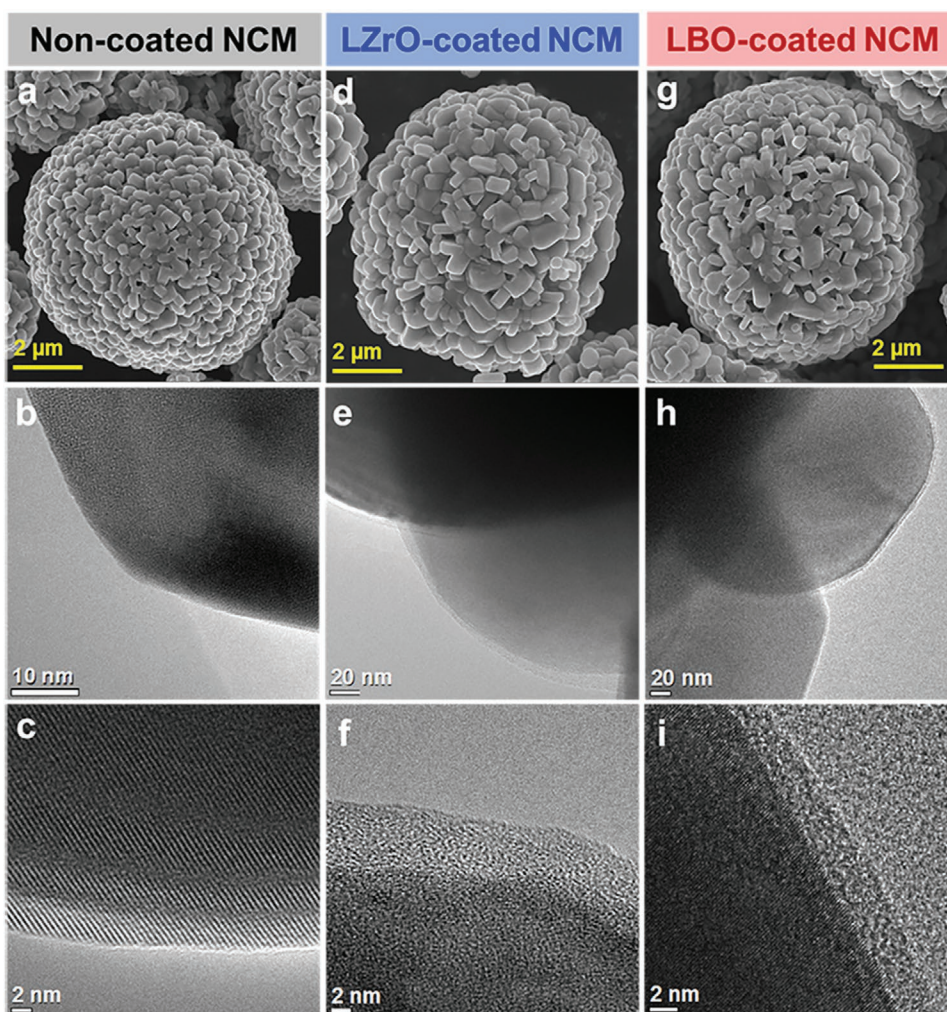


**Figure 2.** SEM, TEM, and HRTEM images of the morphology of uncoated/coated NCM<sup>523</sup> particles: a–c) uncoated NCM<sup>523</sup>, d–f) LZrO-coated NCM<sup>523</sup>, and g–i) LBO-coated NCM<sup>523</sup>. The scale bars are presented individually.

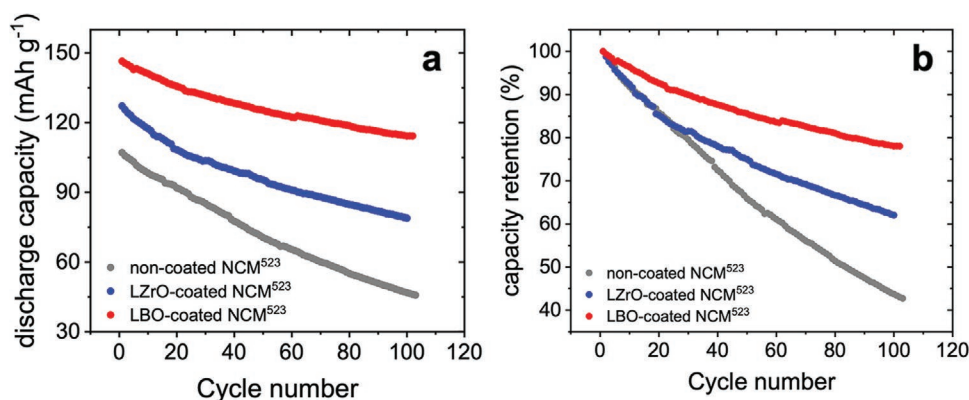


**Figure 3.** Electrochemical cycling of full cells using uncoated (gray), LZrO-coated (blue), and LBO-coated (red) NCM<sup>523</sup> cathodes: a) discharge capacity and b) capacity retention. All the cells were subject to galvanostatic cycling for 100 cycles. LPS (SE) and graphite (anode) powder from the same batch were used in all the cells to maximize consistency.

worst capacity retention (42.7% after 100 cycles). Both coatings improve the full-cell performance, providing larger capacity and higher retention. Compared with the LZrO coating, the LBO coating yields a significantly enhanced discharge capacity (146.5 mAh g<sup>-1</sup> in the 1st cycle) and superior cycling stability (78.0% capacity retention after 100 cycles), suggesting a more effective protection of the NCM<sup>523</sup>/LPS interface. This observation is consistent with our DFT computation, in which LBO is predicted to exhibit excellent chemical compatibility and electrochemical stability at a high cutoff voltage of 4.3 V.

To better understand the electrochemical behavior of NCM<sup>523</sup> with different cathode coatings, (S)TEM was used to investigate the coating integrity and interphase formation during cycling. HRTEM images of the LBO-coated and LZrO-coated NCM<sup>523</sup> in composite cathodes before any electrochemical cycling are presented in Figure 4a,c, respectively. Both the LBO and LZrO coatings are amorphous and intact after mixing with LPS and carbon nanofibers (CNFs). The morphology and amorphous nature of LBO coating remain unchanged after the 1st cycle (Figure 4b). In contrast, after the 1st cycle, the LZrO coating transformed from an amorphous layer into nanocrystalline phases with nonhomogeneous coverage on the surface of the NCM<sup>523</sup> particles, as observed in Figure 4d. As shown in the fast Fourier transform (FFT) image inserted in Figure 4d, the observed nanocrystalline phase can be indexed to the cubic ZrO<sub>2</sub> structure (space group Fm $\bar{3}$ m, inorganic crystal structure database (ICSD) No. 53998). This phase transformation is likely the result of the Li extraction from LZrO under high voltage, consistent with the theoretical prediction expressed by Reaction (1). In fact, ZrO<sub>2</sub> nanocrystals can already be observed in the delithiated state even after initial charging to 4.3 V (Figure S4, Supporting Information). The high-angle annular dark-field scanning transmission electron microscopy (HAADF-STEM) image and energy-dispersive X-ray spectroscopy (EDX) mapping in Figure 4e,f reveal the elemental distribution of Zr and Mn in the LZrO coated NCM<sup>523</sup> after the 1st cycle. In contrast to the homogenous coating of 5 nm thickness observed for the sample before cycling in Figure 4c, the decomposition of LZrO resulted in the formation of an aggregated region of  $\approx$ 70 nm thickness (Figure 4e,f and Figure S4, Supporting Information).

After the LZrO coating breaks down, NCM<sup>523</sup> is likely to be subjected to direct contact with LPS, leading to the formation of a highly unstable interface. The HAADF-STEM image in Figure 5a shows the morphology of the LZrO-coated NCM<sup>523</sup> after the 1st cycle; the surface of NCM<sup>523</sup> is rough and mostly covered by island-like nanocrystals. As observed in the scanning transmission electron microscopy-electron energy loss spectroscopy (STEM-EELS) line scan spectra in Figure 5b,c, inhomogeneous distributions of Ni, Mn, and Co can be observed from the edge to the bulk region. Notably, although signals from Ni and Co are observed in the first few EELS line spectra in Figure 5c (corresponding to the edge of the NCM<sup>523</sup> particle), the signal from oxygen can barely be detected. This result suggests that Ni and Co no longer exist in the oxide form at the very surface and the elemental inhomogeneity is not due to the typical surface segregation and densification observed in layered lithium transition metal oxide cathodes in liquid-electrolyte battery systems.<sup>[26,27]</sup> Overlap of Ni, Co, and S is observed in the EDX mappings in Figure 5e, suggesting the possible presence of transition metal sulfides in the decomposition products.

In contrast to the phase decomposition and aggregation observed in the LZrO-coated sample, the LBO coating remains amorphous and intact even after extended cycling in an SSB. As observed in Figure 6a, the morphology and amorphous nature of the LBO coating are well preserved after ten cycles. A uniform distribution of the LBO coating on the NCM<sup>523</sup> particle after ten cycles is observed in the EDX mappings in Figure 6b,c. More images taken on the same sample are presented in Figure S5 in the Supporting Information. The HAADF-STEM image of the LBO-coated NCM<sup>523</sup> after ten cycles is presented in Figure 6d, with a clean surface of the coated NCM<sup>523</sup> particle observed in the interface region in contact with the LPS particle. With the protection of the intact LBO coating, no interfacial reaction between LPS and NCM<sup>523</sup> is detected in the LBO-coated samples. Homogeneous distributions of different elements are also found in the corresponding EELS line spectra of the LBO-coated NCM<sup>523</sup> sample in Figure 6d,e, indicating the chemical integrity of the NCM<sup>523</sup> particle. The atomic-resolution HAADF-STEM image in Figure 6f shows the crystalline structure of the LBO-coated NCM<sup>523</sup> after ten cycles, in which

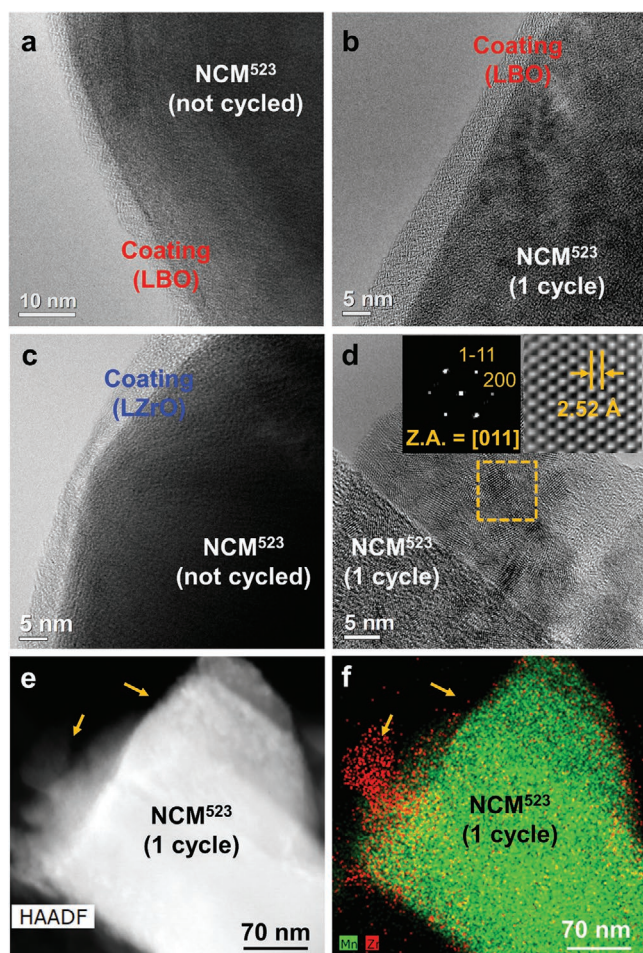
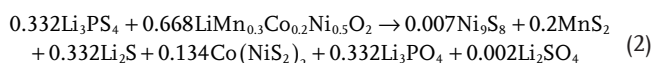


**Figure 4.** Comparison of LZO- and LBO-coated NCM<sup>523</sup> cathode composite prior to electrochemical cycling and after 1st cycle. a) HRTEM image of LBO-coated NCM<sup>523</sup> (mixed with LPS and CNF, prior to electrochemical cycling). b) HRTEM image of LBO coated NCM<sup>523</sup>/LPS/CNF after 1st cycle. c) HRTEM image of LZO-coated NCM<sup>523</sup> (mixed with LPS and CNF, prior to electrochemical cycling). d) HRTEM image of LZO-coated NCM<sup>523</sup>/LPS/CNF after 1st cycle (the FFT inset showing the decomposition product of ZrO<sub>2</sub>). e) HAADF-STEM image and f) elemental mapping of LZO-coated sample after 1st cycle, showing the aggregation of the decomposition product.

the bright and dark columns correspond to atomic columns of transition metal cations and Li-ions, respectively. Interestingly, the Z-contrast difference decreases in the edge region of the NCM<sup>523</sup> crystal compared with that in the bulk region (Figure 6f and Figure S6, Supporting Information). The FFT image of the edge area reveals a rock-salt structure (inset of Figure 6f and Figure S6, Supporting Information), indicating that the surface structure of NCM<sup>523</sup> changed from a layered structure (R $\bar{3}m$ ) to a rock-salt structure (Fm $\bar{3}m$ ), similar to the surface densification reported in liquid-electrolyte battery systems.<sup>[27]</sup> While this may contribute to the observed capacity fade, the LBO coating remains stable with long-term operation as shown by the electron microscopy images of the well-preserved LBO coating after 50 cycles (Figures S7 and S8, Supporting Information).

### 2.3. Interfacial Reaction(s) between NCM<sup>523</sup> and LPS after the LZrO Coating Breakdown

To further investigate the NCM<sup>523</sup>/LPS interparticle interface and decomposition products after breakdown of the LZrO coating, HAADF-STEM and EDX analysis of the LZrO-coated sample after long-term cycling was performed. Figure 7 presents the STEM-EDX analysis of the NCM<sup>523</sup>/LPS particles after 50 cycles. The reaction between NCM<sup>523</sup> and LPS led to the formation of an extended interface region, as observed in Figure 7a. According to the elemental mapping in Figure 7c, the distributions of Ni and Co overlap well in the decomposition region but have become spatially separated from the distribution of Mn (Figure 7b, overlay map of Ni/Mn). The segregation of transition metals into distinct Co–Ni–S and Mn–S domains is consistent with the computational reaction prediction (Reaction (2)), which indicates separate (Co,Ni)-sulfides and Mn-sulfides to form, though the STEM-EDX cannot identify the exact stoichiometry of the reaction products. Notably, some of the predicted decomposition products, such as Co(NiS<sub>2</sub>)<sub>2</sub>, are likely to be electronically conductive.<sup>[22,28–30]</sup> Thus, the electrochemical decomposition of LPS may not be passivated by the chemical reaction between NCM<sup>523</sup> and LPS, leading to a progressive degradation with long-term cycling and significant capacity fade.



## 3. Discussion

While many cathode coating materials have been proposed and tested in SSBs, their effectiveness varies. While a lack of coating stability will influence battery capacity, it is difficult to identify specific mechanisms and severity of degradation from capacity loss with cycling. For this reason we performed a detailed microscopy study and correlated it with predictions that can be made from first principles calculations. The remarkable breakdown of the LZrO coating and the integrity of the LBO coating at high voltages provide strong experimental confirmation of previous theory results and are fully consistent with the idea that the high voltage limit of coating materials is determined by the extent of hybridization of the oxygen anion:<sup>[14]</sup> The strong covalent bonding in the BO<sub>3</sub> and BO<sub>4</sub> groups in Li<sub>3</sub>B<sub>11</sub>O<sub>18</sub> push the oxygen states down in energy, thereby protecting them from oxidation to a much larger extent than in LZrO.

As revealed in this study, the rapid decomposition of the LZrO coating occurs due to Li extraction at high voltage, leading to both morphology and chemical changes of the coating. After Li is extracted, the thin LZrO coating transforms into aggregated regions of a poor Li conductor (ZrO<sub>2</sub>), which further results in inhomogeneous coverage on the NCM<sup>523</sup> particles, exposing them to the LPS surroundings. Decomposition of the LZrO coating was found to continue upon cycling, consistent with the large capacity fade. While S/O exchange is predicted by DFT for an oxide/thiophosphate interface it is remarkable that even at room temperature segregation of transition metals

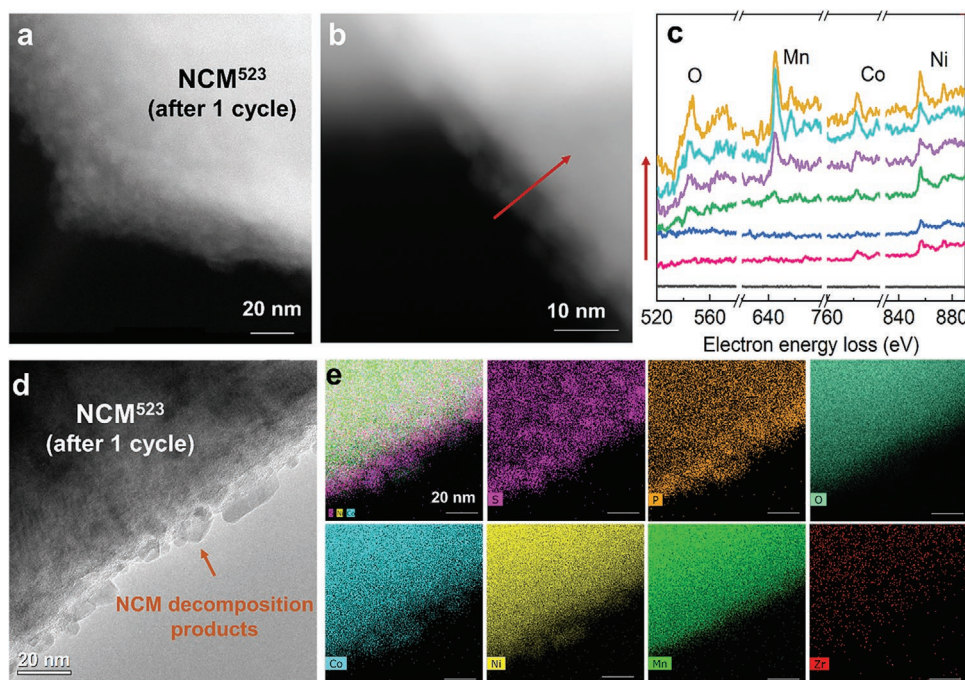


**Figure 5.** LZrO-coated NCM<sup>523</sup> cathode composite after 1st cycle. a,b) HAADF-STEM images of LZrO-coated NCM<sup>523</sup> after one cycle, c) corresponding EELS line scan spectrum, d) TEM image, and e) EDX elemental mappings.

into distinct Co–Ni–S and Mn–S compounds can be identified as products of the reaction between NCM<sup>523</sup> and LPS. The agreement between ab initio computations based on a thermodynamic framework and the experimental observations indicates that even at room temperature near equilibration occurs on a very small scale. In fact, the segregation of Mn was also observed in a charged LiNi<sub>1/3</sub>Co<sub>1/3</sub>Mn<sub>1/3</sub>O<sub>2</sub>–LPS composite after being heated above 300 °C.<sup>[8]</sup> In that study, Tatsumisago and co-workers identified crystalline transition metal sulfides, such as MnS and CoNi<sub>2</sub>S<sub>4</sub>, as well as Li<sub>3</sub>PO<sub>4</sub> using synchrotron X-ray diffraction.<sup>[8]</sup> Our study shows that even at room temperature during normal battery operation the precursors of those crystalline degradation products already form. The oxidation of S<sup>2-</sup> in thiophosphate electrolytes has also been observed in previous X-ray photoelectron spectroscopy studies.<sup>[31,32]</sup>

It should be pointed out that while the key findings presented in this study are based on an SSB system, the electrochemical stability of a coating material is relevant in liquid electrolytes as well. LZrO will be prone to Li extraction under high voltage in both liquid and solid electrolyte. However, a significant difference is that in a solid-state battery the oxygen released from the LZrO decomposition can in turn exchange with the S<sup>2-</sup> in the LPS surroundings, resulting in a decreased local oxygen partial pressure. Whether this low oxygen partial pressure is transmitted through the thin amorphous coating and leads to reductive instability of NCM<sup>523</sup> in a solid-state battery similar to densification in a liquid cell is unclear, but our result that even when the LBO coating remains intact the NCM<sup>523</sup> surface undergoes disordering similar to what is seen in liquid electrolytes, is suggestive. Understanding oxygen transport through cathode coatings should therefore be a topic of investigation.

Our results highlight the importance of electrochemical stability of coating materials in practical applications. An effective coating is important to protect NCM<sup>523</sup> particles from decomposition driven by its reactivity with the solid-state electrolyte. In addition to the (electro-)chemical stability and a reasonably good ionic conductivity, an effective coating should also exhibit good deformability to maintain its morphological integrity for a good contact and homogenous coverage throughout the entire cycle life. As shown in Figure S7 in the Supporting Information, the amorphous LBO coating remains intact on the NCM<sup>523</sup> particles after 50 cycles, allowing an effective protection of the interparticle interface. The soft nature of the lithium borate glass is expected to provide better mechanical “viscosity” on the NCM<sup>523</sup> particles than a mechanically stiff and brittle coating such as LiNbO<sub>3</sub> to accommodate the anisotropic volume expansion and contraction of NCM<sup>523</sup> during lithiation and delithiation.<sup>[13,33]</sup> The presence of a coating also brings new considerations into the cell assembly process and the full-cell fabrication. Ball-milling and/or aggressive grinding during mixing of the coated NCM<sup>523</sup> and LPS tend to break the coated secondary NCM<sup>523</sup> particles and generate new unprotected interfaces. Gentle approaches (e.g., gentle grinding or soft milling) are suggested in the cathode composite mixing process (Figure S9, Supporting Information).

Although direct observations from electron microscopy have provided valuable information on the composition, nanosized crystalline structure, and surface/interface morphology of the interfaces, isolating an intact solid interface and characterizing the spatial degradation of the amorphous electrolyte still remains challenging in SSBs. For example, although decomposition appears in a region of ≈200 nm in thickness in Figure 7a, the diffusion distance cannot be accurately determined as the spatial distribution of particles cannot be preserved during the

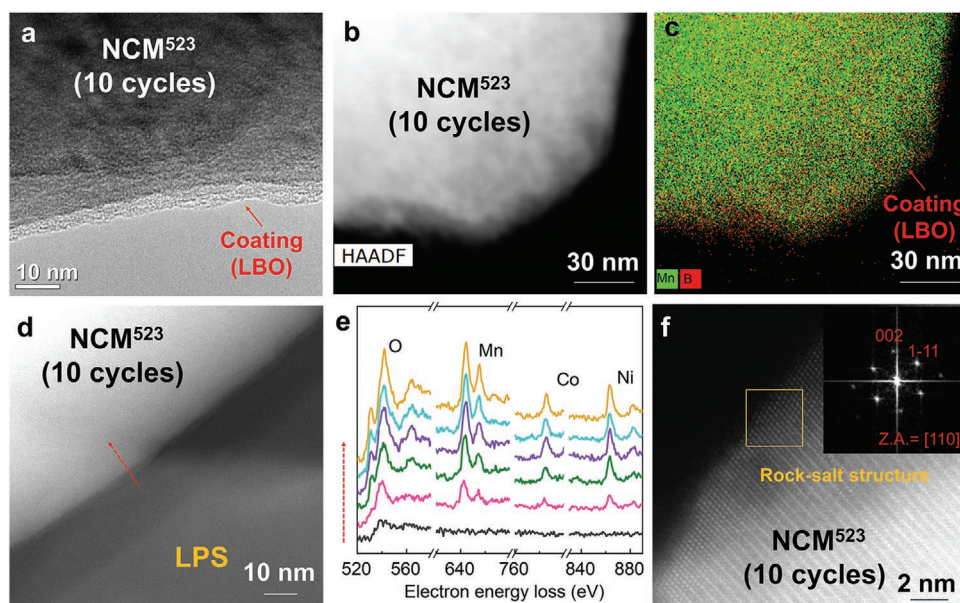


**Figure 6.** LBO-coated NCM<sup>523</sup> cathode composite after ten cycles. a) HRTEM image, b) HAADF-STEM image, and c) elemental mapping of LBO-coated NCM<sup>523</sup>. d) HAADF-STEM image of LBO-coated NCM<sup>523</sup> with LPS interface with corresponding e) line scan EELS spectrum from surface of LBO-coated NCM<sup>523</sup> to the bulk after ten cycles shown in (d). f) high-resolution STEM image of LBO coated NCM<sup>523</sup> after ten cycles.

sonication process of the sample preparation. Precise cutting of the buried cathode/interface cross-section is needed for better sample preparation. Combining various microscopy technique, such as scanning transmission X-ray microscopy, together with analytical electron microscopy is also desired in future studies to probe how the electronic and chemical structure of the solid electrolyte interface evolve in dynamic electrochemical process.<sup>[34,35]</sup>

## 4. Conclusion

In this work, we combined ab initio computation with electron microscopy investigations to identify lithium borate LBO as a promising coating for the thiophosphate system and explain its superior performance. Both DFT calculation and microscopic characterization suggest excellent chemical and oxidation stability of the LBO coating in an NCM<sup>523</sup>–LPS cathode composite, effectively suppressing interfacial reactions, providing significantly higher capacity and enhanced capacity retention in a full-cell SSB. Direct observations from TEM and STEM reveal that LZrO is not stable at high voltages and is not effective for protecting the NCM<sup>523</sup> cathode. This work elucidates the critical parameters required for cathode coatings and provides insight into the design of coatings for high-voltage SSBs.

## 5. Experimental Section

**Electrochemical Stability Calculation:** The electrochemical stability window is calculated using the grand potential method developed in previous work.<sup>[5,24,36]</sup> All the DFT data are obtained from the Materials Project database.<sup>[37]</sup>

The topotactic Li extraction voltage (kinetic stability limit) is calculated as the energy of removing one Li atom from a supercell with at least

16 formula units.<sup>[25]</sup> The DFT calculations were performed in Perdew–Burke–Ernzerhof generalized gradient approximation as implemented in the Vienna ab initio simulation package.<sup>[37,38,39]</sup> The interactions between ion cores and valence electrons are described using the projector augmented wave method with a plane-wave energy cutoff of 520 eV and a *k*-point density of at least 1000/*n*<sub>atom</sub>.<sup>[40]</sup> All supercells were fully relaxed in the DFT calculations.

The chemical reaction energy at the solid/solid interfaces (cathode/SE, cathode/coating, and SE/coating interfaces) is calculated using the methodology developed by Richards et al. with DFT data obtained from the Materials Project.<sup>[5,37]</sup> The interface reaction calculation functionality is available through the Interface Reactions App of the Materials Project website.<sup>[37]</sup>

**Materials Synthesis and Coating Method:** The coated NCM<sup>523</sup> samples were prepared using the sol–gel method reported in previous work.<sup>[41]</sup> For the LBO-coated NCM<sup>523</sup> sample (0.5 mol % LBO coated NCM<sup>523</sup>), the LBO coating solution was first prepared by dissolving stoichiometric amount of Li acetate and triisopropyl borate in super dehydrated ethanol at 60 °C. Next, the NCM<sup>523</sup> powder was dispersed in the as-prepared coating solution with stirring. Then, the solvent from the flask was removed using a rotary evaporator in a hot water bath (60 °C) with ultrasound sonication, followed by a heat treatment at 350 °C. The LZrO-coated NCM<sup>523</sup> (0.5 mol%) sample was prepared using a similar process. Details of the material synthesis and coating process are reported in ref. [41].

**Electron Microscopy Experiments:** Sample preparation was performed in an Ar-filled glove box (water vapor <2 ppm and oxygen <0.1 ppm). The coated/uncoated cathodes were extracted from disassembled cells. The composite cathodes powders were diluted in hexane and sonicated to obtain good particle dispersion. The TEM samples were prepared by drop casting the solution onto a standard 400 copper mesh TEM grid with lacey carbon support. The samples were loaded into a Gatan 648 double-tilt vacuum-transfer holder to transfer the sample from the glovebox to the microscope in an inert Ar atmosphere. The HRTEM and STEM-EDX characterizations were performed using an FEI TitanX 60-300 microscope. For each sample, more than 20 interfacial regions have been examined from different LZrO or LBO coated primary particles. The electron beam currents were carefully controlled during imaging



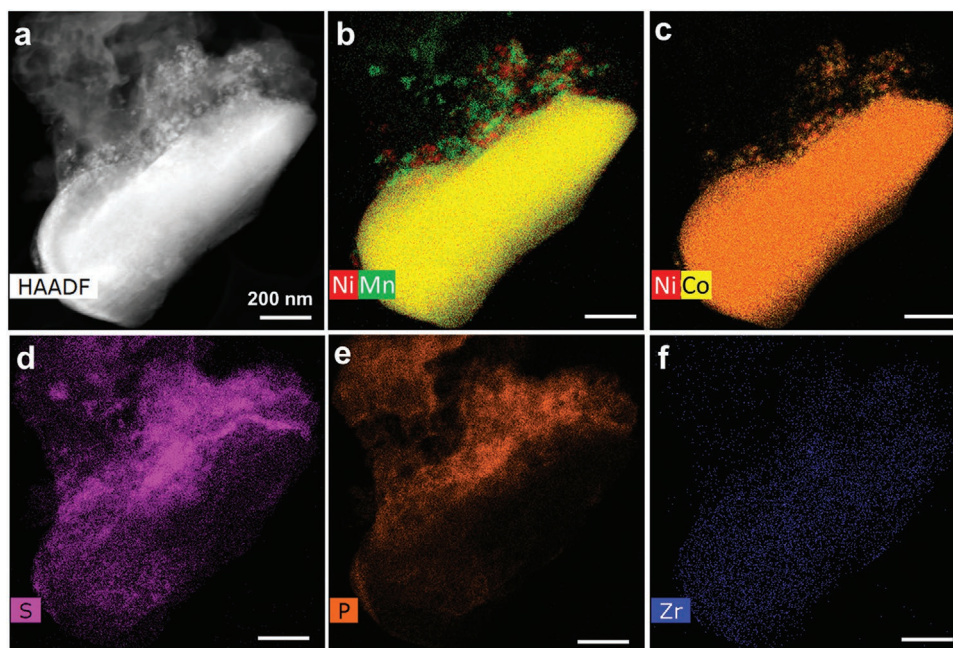


**Figure 7.** LzrO-coated NCM<sup>523</sup> cathode composite after 50 cycles. a) HAADF-STEM image and b–f) EDX elemental mappings.

to prevent electron irradiation damage to the samples. The stability of NCM<sup>523</sup>/LPS interface before and after imaging were evaluated, with the HAADF-STEM images before and after EDX mapping shown in Figure S10 in the Supporting Information. The high-resolution STEM and EELS analyses were performed using the TEAM I microscope (a modified FEI Titan 80-300 microscope with double-aberration-corrected (scanning) transmission electron microscope). SEM images were obtained on a Zeiss Gemini Ultra-55 analytical field-emission scanning electron microscope at the Molecular Foundry at Lawrence Berkeley National Laboratory (LBNL).

**Electrochemical Characterization:** Full cells using uncoated or LzrO/LBO-coated NCM<sup>523</sup> as the cathode, LPS as the bulk SE, and graphite as the anode/reference electrode were constructed and cycled at a constant current (0.1 mA cm<sup>-2</sup> for charge and 0.05 mA cm<sup>-2</sup> for discharge). Both cathode and anode composites contained 60% active material, 35% LPS, and 5% CNF were prepared through gentle hand grinding. The cells were assembled under an Ar atmosphere using otherwise identical procedure and LPS powder from the same batch to maximize consistency. To prepare the full-cell SSBs, ≈100 mg of LPS powder was cold pressed into a loose “pellet” under small pressure. Then, 10 mg of the cathode composite powders and anode composite powders were carefully added to both sides of the LPS pellet before applying a pressure of ≈350 MPa for 5 min within an in-house-designed pressure cell (13 mm inner diameter) in an Ar-filled glovebox. A pressure of 5 MPa was applied to the cells during cycling. All the electrochemical tests were conducted at room temperature under Ar atmosphere.

characterizations were performed at the Molecular Foundry at LBNL, supported by the Office of Science, Office of Basic Energy Sciences, of the U.S. Department of Energy under Contract No. DE-AC02-05CH11231. This research used resources of the National Energy Research Scientific Computing Center (NERSC), a U.S. Department of Energy Office of Science User Facility operated under Contract No. DE-AC02-05CH11231. This work also used the Extreme Science and Engineering Discovery Environment (XSEDE) supported by National Science Foundation under Grant No. ACI-1548562.

## Conflict of Interest

The authors declare no conflict of interest.

## Keywords

all-solid-state batteries, cathode coatings, DFT calculations, interfacial stability, microscopy observations

Received: November 17, 2019

Revised: May 5, 2020

Published online: June 5, 2020

## Supporting Information

Supporting Information is available from the Wiley Online Library or from the author.

## Acknowledgements

Y.-Q.Z and Y.T. contributed equally to this work. This work was supported by the Samsung Advanced Institute of Technology. The TEM and SEM

- [1] A. Manthiram, X. Yu, S. Wang, *Nat. Rev. Mater.* **2017**, *2*, 16103.
- [2] J. Li, C. Ma, M. Chi, C. Liang, N. J. Dudney, *Adv. Energy Mater.* **2015**, *5*, 1401408.
- [3] Y. Kato, S. Hori, T. Saito, K. Suzuki, M. Hirayama, A. Mitsui, M. Yonemura, H. Iba, R. Kanno, *Nat. Energy* **2016**, *1*, 16030.
- [4] F. P. McGrogan, T. Swamy, S. R. Bishop, E. Eggleton, L. Porz, X. Chen, Y. M. Chiang, K. J. Van Vliet, *Adv. Energy Mater.* **2017**, *7*, 1602011.
- [5] W. D. Richards, L. J. Miara, Y. Wang, J. C. Kim, G. Ceder, *Chem. Mater.* **2016**, *28*, 266.

- [6] H. Kitaura, A. Hayashi, K. Tadanaga, M. Tatsumisago, *Electrochim. Acta* **2010**, *55*, 8821.
- [7] A. Sakuda, A. Hayashi, M. Tatsumisago, *Chem. Mater.* **2010**, *22*, 949.
- [8] H. Tsukasaki, T. Uchiyama, K. Yamamoto, S. Mori, Y. Uchimoto, H. Kowada, A. Hayashi, M. Tatsumisago, *J. Power Sources* **2019**, *434*, 226714.
- [9] W. Fitzhugh, F. Wu, L. Ye, W. Deng, P. Qi, X. Li, *Adv. Energy Mater.* **2019**, *9*, 1900807.
- [10] A. M. Nolan, Y. Zhu, X. He, Q. Bai, Y. Mo, *Joule* **2018**, *2*, 2016.
- [11] L. Xu, S. Tang, Y. Cheng, K. Wang, J. Liang, C. Liu, Y. C. Cao, F. Wei, L. Mai, *Joule* **2018**, *2*, 1991.
- [12] W. Zhang, F. H. Richter, S. P. Culver, T. Leichtweiss, J. G. Lozano, C. Dietrich, P. G. Bruce, W. G. Zeier, J. Janek, *ACS Appl. Mater. Interfaces* **2018**, *10*, 22226.
- [13] S. P. Culver, R. Koerver, W. G. Zeier, J. Janek, *Adv. Energy Mater.* **2019**, *9*, 1900626.
- [14] Y. Xiao, L. J. Miara, Y. Wang, G. Ceder, *Joule* **2019**, *3*, 1252.
- [15] G. Oh, M. Hirayama, O. Kwon, K. Suzuki, R. Kanno, *Chem. Mater.* **2016**, *28*, 2634.
- [16] K. H. Park, D. Y. Oh, Y. E. Choi, Y. J. Nam, L. Han, J. Y. Kim, H. Xin, F. Lin, S. M. Oh, Y. S. Jung, *Adv. Mater.* **2016**, *28*, 1874.
- [17] K. Takada, N. Ohta, L. Zhang, K. Fukuda, I. Sakaguchi, R. Ma, M. Osada, T. Sasaki, *Solid State Ionics* **2008**, *179*, 1333.
- [18] J. W. Lee, Y. J. Park, *J. Electrochem. Sci. Technol.* **2018**, *9*, 176.
- [19] S. Ito, S. Fujiki, T. Yamada, Y. Aihara, Y. Park, T. Y. Kim, S.-W. Baek, J.-M. Lee, S. Doo, N. Machida, *J. Power Sources* **2014**, *248*, 943.
- [20] T. Minami, *Solid State Ionics for Batteries*, Springer Science & Business Media, Heidelberg **2006**.
- [21] Y. Zhu, X. He, Y. Mo, *J. Mater. Chem. A* **2016**, *4*, 3253.
- [22] S. H. Jung, K. Oh, Y. J. Nam, D. Y. Oh, P. Brüner, K. Kang, Y. S. Jung, *Chem. Mater.* **2018**, *30*, 8190.
- [23] S. Choi, B. N. Yun, W. D. Jung, T. H. Kim, K.-Y. Chung, J. W. Son, B. I. Sang, H. G. Jung, H. Kim, *Scr. Mater.* **2019**, *165*, 10.
- [24] S. P. Ong, Y. Mo, W. D. Richards, L. Miara, H. S. Lee, G. Ceder, *Energy Environ. Sci.* **2013**, *6*, 148.
- [25] Y. Tian, T. Shi, W. D. Richards, J. Li, J. C. Kim, S. H. Bo, G. Ceder, *Energy Environ. Sci.* **2017**, *10*, 1150.
- [26] F. Lin, I. M. Markus, D. Nordlund, T. C. Weng, M. D. Asta, H. L. Xin, M. M. Doeff, *Nat. Commun.* **2014**, *5*, 3529.
- [27] S. Hwang, W. Chang, S. M. Kim, D. Su, D. H. Kim, J. Y. Lee, K. Y. Chung, E. A. Stach, *Chem. Mater.* **2014**, *26*, 1084.
- [28] C. Wagner, *Prog. Solid State Chem.* **1975**, *10*, 3.
- [29] J. Yang, C. Bao, K. Zhu, T. Yu, F. Li, J. Liu, Z. Li, Z. Zou, *Chem. Commun.* **2014**, *50*, 4824.
- [30] S. C. Han, H. S. Kim, M. S. Song, J. H. Kim, H. J. Ahn, J. Y. Lee, *J. Alloys Compd.* **2003**, *351*, 273.
- [31] F. Walther, R. Koerver, T. Fuchs, S. Ohno, J. Sann, M. Rohnke, W. G. Zeier, J. Janek, *Chem. Mater.* **2019**, *31*, 3745.
- [32] R. Koerver, I. Aygün, T. Leichtweiß, C. Dietrich, W. Zhang, J. O. Binder, P. Hartmann, W. G. Zeier, J. Janek, *Chem. Mater.* **2017**, *29*, 5574.
- [33] M. Gruber, A. Leitner, D. Kiener, P. Supancic, R. Bermejo, *Mater. Des.* **2018**, *153*, 221.
- [34] D. Qian, C. Ma, K. L. More, Y. S. Meng, M. Chi, *NPG Asia Mater.* **2015**, *7*, e193.
- [35] Z. Wang, Y. S. Meng, in *Handbook of Solid State Batteries*, World Scientific, Singapore **2016**.
- [36] Y. Tian, Y. Sun, D. C. Hannah, Y. Xiao, H. Liu, K. W. Chapman, S. H. Bo, G. Ceder, *Joule* **2019**, *3*, 1037.
- [37] A. Jain, S. P. Ong, G. Hautier, W. Chen, W. D. Richards, S. Dacek, S. Cholia, D. Gunter, D. Skinner, G. Ceder, *APL Mater.* **2013**, *1*, 011002.
- [38] J. P. Perdew, K. Burke, M. Ernzerhof, *Phys. Rev. Lett.* **1996**, *77*, 3865.
- [39] G. Kresse, J. Furthmüller, *Comput. Mater. Sci.* **1996**, *6*, 15.
- [40] P. E. Blöchl, *Phys. Rev. B* **1994**, *50*, 17953.
- [41] M. Agostini, U. Ulissi, D. Di Lecce, Y. Ahiara, S. Ito, J. Hassoun, *Energy Technol.* **2015**, *3*, 632.